Dependency of mesoscale organization on grid anisotropy in large-eddy simulations of convective boundary layers at Gray Zone resolutions.

Stephan R. de Roode[1], A. Pier Siebesma[1,2], Fredrik Jansson[1], Martin Janssens[1,3]

[1]Delft University of Technology, Delft, Netherlands
[2]KNMI, De Bilt, Netherlands
[3]Wageningen University, Wageningen, Netherlands

Key Points:

- A grid anisotropy factor is introduced to efficiently switch from an isotropic to an anisotropic eddy diffusion approach for large-eddy simulation models.
- The organization of clear boundary-layer convection depends on the horizontal grid spacings, most notably for the anisotropic eddy diffusion approach.
- Reduced variances at the smallest length scales may be compensated by opposite increases at larger length scales.

Corresponding author: SR de Roode, s.r.deroode@tudelft.nl

Abstract

A new generation of operational atmospheric models operating at horizontal resolutions in the range 200 m $\sim$ 2 km is becoming increasingly popular for operational use in numerical weather prediction and climate applications. Such grid spacings are becoming sufficiently fine to resolve a fraction of the turbulent transports. Here we analyze LES results of a convective boundary layer obtained by coarsening horizontal grid spacings up to 800 m. The aim is to explore the dependency of the mean state and turbulent fluxes on the grid resolution. Both isotropic and anisotropic eddy diffusion approaches are evaluated, where in the latter case the horizontal and vertical eddy diffusivities differ in accord with their horizontal and vertical grid spacings. For coarsening horizontal grid sizes entrainment at the top of the boundary layer tends to get slightly enhanced for isotropic diffusion. An analysis of the energy spectrum shows that anisotropic diffusion causes relatively more dissipation of variance at smaller length scales. This leads, in turn, to a shift of spectral energy towards larger length scales. This can also be clearly seen from the different kinds of spatial organization. The present study therefore suggests that details with regards to the representation of processes at small scales might impact the organization at length scales much larger than the smallest scales that can be resolved by the model.

Plain Language Summary

A new generation of operational atmospheric models operating at horizontal resolutions in the range 200 m $\sim$ 2 km is becoming increasingly popular for operational use in numerical weather prediction and climate applications. Owing to the ever increasing computational power their grid spacings are nowadays becoming sufficiently fine to allow for resolving a fraction of the turbulent transports. However, these types of models are operated with grid spacings that are much larger in the horizontal directions than in the vertical direction. In the present study we explore the extent to which the organization of turbulence structures is affected by the size of the horizontal grid spacing. This question is addressed by means of large-eddy simulation, which is an established modeling technique that has been designed specifically to resolve the dominant turbulent eddies at a high spatial resolution. It is found that differences in the way how turbulence at scales smaller than the grid spacing is calculated can have an effect on the organization of turbulent structures at much larger spatial scales.

1 Introduction

Numerical simulations of atmospheric turbulence can be performed with models whose spatial resolutions are sufficiently fine to resolve the dominant turbulent eddies. Large-eddy simulation (LES) is an important and widely used technique in this respect. LES is nowadays used to successfully reproduce a wide range of atmospheric flow regimes including the transition from a stable to a convective boundary layer (van Hooft et al., 2019), shallow and deep convective clouds (Wing et al., 2020), as well as flows in urban areas (Grylls et al., 2020; Hellsten et al., 2020). The skill with which they can faithfully capture observations has been addressed in various model intercomparison studies including the clear convective boundary layer (Nieuwstadt et al., 1993), the stable boundary layer (Beare et al., 2006), precipitating shallow cumulus (VanZanten et al., 2011), and the transition of stratocumulus to shallow cumulus (Van der Dussen et al., 2013). As a result LES is becoming an increasingly more powerful tool for operational use in weather and climate applications and are used as high resolution limited area models embedded in larger scale atmospheric models (Schalkwijk et al., 2015; Heinze et al., 2017; Draxl et al., 2021).

LES models do often apply anisotropic grids, with the horizontal grid spacing typically much coarser than the vertical, $\Delta x_{\mathrm{hor}} > \Delta z$. Such a choice is motivated by the

need, on the one hand, to resolve sharp vertical gradients such as present near the ground surface and thermal inversion layers, and, on the other hand, to capture a sufficient number of large eddies in the LES domain. For example, LES models that participated in the model intercomparison study of a convective boundary layer by Nieuwstadt et al. (1993) applied horizontal and vertical domain sizes $L_{\rm hor} = 6400$ m and $L_{\rm ver} = 2400$ m, respectively, and $\Delta x_{\rm hor} = 160$ m and vertical grid spacings as fine as 20 m near the surface.

The contribution of the unresolved eddies to the turbulent transports as well as their dissipation by molecular viscosity can be parameterized in LES models with use of a parameterized subgrid turbulent kinetic energy (TKE) model. The subgrid turbulent fluxes are typically taken to be proportional to an eddy diffusivity factor, which depends on the intensity of the unresolved velocity fluctuations as quantified by the subgrid TKE, and a turbulent length scale that depends on the horizontal and vertical grid spacings (Deardorff, 1980b). Even though the grid may be anisotropic, LES models may apply an isotropic diffusion approach. The latter means that they apply an equal value for the eddy diffusion in all the three directions, as opposed to an anisotropic diffusion approach in which the eddy diffusivity is taken directionally dependent.

The supercomputing facilities nowadays allow operating numerical global weather forecast models at sub-kilometer scales, which enables them to resolve some fraction of the turbulent eddies. In the latter case parameterizations that were developed for turbulent transport in large-scale models need to be adapted, basically because the implicit assumption that the turbulent transports are entirely due to the unresolved, subgrid fluctuations becomes violated (Honnert et al., 2020). This question has motivated Boutle et al. (2014) to design a new scale-aware parameterization that is in part inspired by LES subgrid TKE models.

In the present study we investigate the behaviour of the isotropic and anisotropic diffusion approaches for coarsening horizontal grid sizes, towards values that are currently feasible for NWP models. Because subgrid diffusion tends to smooth out resolved fluctuations at the smallest length scales, we are particularly interested in the question as to how this affects the energy spectra and the organization of turbulence structures. To this end, we simulated a clear convective boundary layer with the Dutch Atmospheric Large Eddy Simulation (DALES) model (Heus et al., 2010; Arabas et al., 2021) with horizontal grid spacings ranging from isotropic to extremely anisotropic, $\Delta x_{\rm hor} = 12.5$ and 800 m, respectively. Section 2 will introduce a grid anisotropy factor that can be used to efficiently switch from an isotropic to an anisotropic diffusion approach, with the latter quite similar to what is applied by the System for Atmospheric Modeling (SAM) LES model (Stevens et al., 2005). The case set up is briefly explained in Section 3, next the results are presented and discussed in Section 4, and Section 5 gives a summary and conclusions.

2 A comparison of the isotropic and anistropic subgrid diffusion approaches

Here we will consider an anisotropic grid which has the same size $\Delta x_{\rm hor}$ in both horizontal directions, $\Delta x = \Delta y = \Delta x_{\rm hor}$, but whose vertical mesh size is smaller than the horizontal ones, a configuration that is typical for LES applications of atmospheric systems, $\Delta x_{\rm hor} \geq \Delta z$. As opposed to the isotropic diffusion approach, an anisotropic subgrid scheme applies an eddy viscosity, and similarly an eddy diffusivity, that depends on the direction to which it is applied, with its magnitude being dependent on the grid spacing in the respective direction. Here we will compare the isotropic subgrid diffusion scheme as proposed by Deardorff (1980a) with an anisotropic diffusion approach that is, as an example, applied in the System for Atmospheric Modeling (SAM) LES model (Stevens et al., 2005; Khairoutdinov & Randall, 2005).

Although the eddy diffusivity and viscosity are different quantities that are applied to scalars and momentum, respectively, we will sometimes loosely refer to both of them simply as the eddy diffusivity.

2.1 LES budget equations

Models that are applied to simulating atmospheric motions apply the conservation equations of momentum, heat, and the total water specific humidity, which can generally be expressed as

$$\frac{d\varphi}{dt} = \frac{\partial \varphi}{\partial t} + u_j \frac{\partial \varphi}{\partial x_j} = S_\varphi, \tag{1}$$

with t the time, φ an arbitrary prognostic variable, the velocity vector components $(u_1, u_2, u_3) = (u, v, w)$ in the (x, y, z) direction, respectively, with z the vertical direction, and S_φ a source term. LES models apply filtered equations in which the prognostic variables are decomposed in so-called resolved ($\tilde{\varphi}$) and subgrid fluctuations (φ''), i.e. $\varphi = \tilde{\varphi} + \varphi''$ (Leonard, 1974). The subgrid fluctuations are associated with unresolved structures that have length scales that are close to the applied grid spacing. Application of the filter to the conservation equation (1) gives

$$\frac{\partial \tilde{\varphi}}{\partial t} = -\frac{1}{\rho_0}\frac{\partial \rho_0 \tilde{u}_j \tilde{\varphi}}{\partial x_j} - \frac{1}{\rho_0}\frac{\partial \rho_0 \widetilde{u_j'' \varphi''}}{\partial x_j} + \tilde{S}_\varphi, \tag{2}$$

where the conservation equation for mass is applied to express the advection term in flux form. Here $\rho_0(z)$ is the reference density profile. The filter operation gives rise to the second term on the right-hand side, which represents the effect of subgrid-scale flux transport. Following the downgradient diffusion approach it is computed for scalars as

$$\widetilde{u_j'' \varphi''} = -K_\mathrm{h} \frac{\partial \tilde{\varphi}}{\partial x_j}, \tag{3}$$

with K_h the eddy diffusivity, whereas the subgrid momentum fluxes depend on the eddy viscosity K_m according to,

$$\widetilde{u_i'' u_j''} = -K_\mathrm{m} \left(\frac{\partial \tilde{u}_i}{\partial x_j} + \frac{\partial \tilde{u}_j}{\partial x_i} \right), \tag{4}$$

with

$$K_\mathrm{m,h} = c_\mathrm{m,h} \sqrt{e} \ell. \tag{5}$$

Here ℓ is a length scale and $c_\mathrm{m,h}$ is a proportionality constant that is applied to a scalar (c_h) or momentum (c_m). They are related through the turbulent Prandtl number according to $\mathrm{Pr} = c_\mathrm{m}/c_\mathrm{h}$. The filtered subgrid TKE (e) can, in turn, be computed from its budget equation (Deardorff, 1980a),

$$\frac{\partial e}{\partial t} + \frac{1}{\rho_0}\frac{\partial \rho_0 \tilde{u}_j e}{\partial x_j} = \frac{g}{\theta_0}\widetilde{w'' \theta_\mathrm{v}''} - \widetilde{u_i'' u_j''}\frac{\partial \tilde{u}_i}{\partial x_j} - \frac{1}{\rho_0}\frac{\partial}{\partial x_j}\left(\rho_0 \widetilde{u_j'' e} + \widetilde{u_j'' p''} \right) - \epsilon, \tag{6}$$

with θ_v the virtual potential temperature, θ_0 the reference profile of the virtual potential temperature, p the pressure and ϵ the viscous dissipation term.

The subgrid buoyancy and momentum fluxes are computed from Eqs. (3) and (4), respectively. Likewise, the total subgrid turbulent transport term is also computed from a downgradient diffusion approach,

$$\widetilde{u_j'' e} + \frac{\widetilde{u_j'' p''}}{\rho_0} = -2K_\mathrm{m}\frac{\partial e}{\partial x_j}. \tag{7}$$

The viscous dissipation term ϵ is calculated as

$$\epsilon = c_\epsilon \frac{e^{3/2}}{\lambda_\epsilon}, \tag{8}$$

with c_ϵ a proportionality constant and λ_ϵ a length scale. The values of the subgrid constants as applied in DALES are summarized in De Roode et al. (2017).

2.1.1 Isotropic diffusion approach

The isotropic diffusivity approach uses $\ell = \lambda_\epsilon = l_\Delta$ (Deardorff, 1980a), with

$$l_\Delta \equiv (\Delta x \Delta y \Delta z)^{1/3}, \tag{9}$$

to give

$$K_{\mathrm{m,h}} = c_{\mathrm{m,h}} l_\Delta \sqrt{e}. \tag{10}$$

It follows from the definition (9) that an anistropic grid spacing has an implicit impact on the subgrid diffusion. For example, a stretching of the horizontal grid spacing causes l_Δ to increase, and this will consequently lead to an increase of $K_{\mathrm{m,h}}$. This implies that the eddy diffusivity, if it is applied isotropically, will also be enhanced for the vertical subgrid eddy transport even if the vertical grid spacing is not modified.

2.1.2 Anisotropic diffusion approach

Here we adopt the anisotropic diffusion approach used in the SAM LES model as described in the Appendix A of Stevens et al. (2005). The eddy diffusivity that is applied in the vertical direction uses Δz as a length scale, which gives

$$K_{\mathrm{m,h,vert}} = c_{\mathrm{m,h}} \Delta z \sqrt{e}. \tag{11}$$

The horizontal eddy diffusivity $K_{\mathrm{m,h,hor}}$ is computed by multiplying $K_{\mathrm{m,h,vert}}$ by a square of the ratio of horizontal to vertical grid spacings,

$$K_{\mathrm{m,h,hor}} = K_{\mathrm{m,h,vert}} \left(\frac{\Delta x_{\mathrm{hor}}}{\Delta z} \right)^2. \tag{12}$$

Following the SAM LES model formulation, the length scale that is used to compute the subgrid TKE is based on the size of the minimum grid spacing in all the three directions. Because it is common practice in atmospheric LES applications to apply a mesh with $\Delta z \leq \Delta x_{\mathrm{hor}}$, such a configuration will be assumed in the remainder of the text. This implies that the subgrid TKE is computed according to Eq. (6) with $\ell = \lambda_\epsilon = \Delta z$, and with an isotropic eddy diffusivity that depends on this length scale as $K_{\mathrm{m,h}} = c_{\mathrm{m,h}} \Delta z \sqrt{e}$.

2.2 Analytical solutions for the eddy diffusivity

In the following we will compare the analytical solutions for the isotropic and anistropic eddy diffusivities under the assumption of a balance between subgrid TKE production by shear and buoyancy, and a loss by viscous dissipation. These three terms comprise the Smagorinsky subgrid model with stability correction (Mason, 1989), which assumes a steady state for e and ignores the mean advection and total turbulent transport of subgrid TKE. In the analytical solutions we will apply the following definitions for the resolved flow rate of strain tensor S and the Brunt-Väisälä frequency N, respectively,

$$S^2 \equiv \frac{1}{2} \left(\frac{\partial u_j}{\partial x_i} + \frac{\partial u_i}{\partial x_j} \right)^2 \tag{13}$$

$$N \equiv \left(\frac{g}{\theta_0} \frac{\partial \theta_{\mathrm{v}}}{\partial z} \right)^{1/2}. \tag{14}$$

The Smagorinsky subgrid TKE equation with buoyancy production can then be expressed as

$$-K_{\mathrm{h}} N^2 + K_{\mathrm{m}} S^2 - c_\epsilon \frac{e^{3/2}}{\lambda_\epsilon} = 0. \tag{15}$$

For an easy comparison of the analytical solutions we introduce a factor r that gives a measure of the grid anisotropy,

$$r \equiv \frac{\Delta x_{\mathrm{hor}}}{\Delta z}. \tag{16}$$

2.2.1 Isotropic diffusion

For the Smagorinsky model including buoyancy production, and with aid of the anistropy factor r, analytical solutions for the subgrid TKE and eddy diffusivity can be expressed as, respectively,

$$e = C_{\mathrm{stab}}\, r^{4/3} \Delta z^2 S^2, \tag{17}$$

$$K_{\mathrm{m,h}} = c_{\mathrm{m,h}} C_{\mathrm{stab}}^{1/2}\, r^{4/3} \Delta z^2 S. \tag{18}$$

with C_{stab} a factor that involves the subgrid model constants and which depends on the local stability as measured by N^2/S^2,

$$C_{\mathrm{stab}} = \frac{c_{\mathrm{m}}}{c_\epsilon}\left(1 - \frac{c_{\mathrm{h}}}{c_{\mathrm{m}}}\frac{N^2}{S^2}\right). \tag{19}$$

It is clear that an increase in the grid anisotropy factor r will yield a larger eddy diffusivity.

2.2.2 Anisotropic diffusion

The analytical solution for the subgrid TKE reads

$$e = C_{\mathrm{stab}} \Delta z^2 S^2, \tag{20}$$

which can be used to express the vertical and horizontal diffusivities as, respectively,

$$K_{\mathrm{m,h,vert}} = c_{\mathrm{m,h}} C_{\mathrm{stab}}^{1/2} \Delta z^2 S, \tag{21}$$

$$K_{\mathrm{m,h,hor}} = c_{\mathrm{m,h}} C_{\mathrm{stab}}^{1/2} r^2 \Delta z^2 S. \tag{22}$$

A comparison of the solutions (18) and (21) shows that for $r > 1$, or equivalently $\Delta x_{\mathrm{hor}} > \Delta z$, the anistropic vertical diffusivity is smaller than the isotropic value. By contrast, a stretching of the horizontal grid spacing will yield a larger diffusivity to be applied in the horizontal direction (22) as compared to the isotropic diffusivity (18). The anisotropic diffusion approach seems physically more appealing as the diffusion that is applied in the vertical direction is not affected by a coarsening of the horizontal grid spacing.

2.2.3 Practical implementation

The original DALES code has been elaborated with the anisotropic diffusion approach with just a few minor modifications at two parts. The first change involves the choice of the length scale to be used in the subgrid TKE equation. We use either $\ell = \lambda_\epsilon = l_\Delta$ as a length scale to compute the isotropic diffusivity, or otherwise $\ell = \lambda_\epsilon = \Delta z$ to give the vertical anisotropic diffusivity. The second change involves a multiplication of the horizontal subgrid fluxes that are present in the budget equations for the prognostic variables with the grid anisotropy factor r^2. This gives the desired enhancement of the horizontal diffusivity for the anistropic diffusion approach. However, to allow for a correct application of the same model code the factor r is purposely set to unity for the isotropic diffusion approach.

3 Set up of the experiments

To compare the performance of the isotropic and anisotropic diffusion approaches we have performed runs of a clear convective boundary layer. Similar to the Grey Zone LES numerical experiments that were carried out by Efstathiou et al. (2016) and Doubrawa & Muñoz-Esparza (2020), sensitivity experiments were performed in which the horizontal grid spacing was systematically coarsened. The setup of the simulations is presented below.

isotropic diffusion	anisotropic diffusion	Δx_{hor} m	anisotropy factor $r = \Delta x_{\mathrm{hor}}/\Delta z$
H289	-	12.5	1
H410	H420	25	2
H411	H421	50	4
H412	H422	100	8
H413	H423	200	16
H414	H424	400	32
H415	H425	800	64

Table 1. Summary of the horizontal grid spacings Δx_{hor} applied in the large-eddy simulations. For all the simulations the vertical grid spacing $\Delta z = 12.5$ m, and the horizontal and vertical domain sizes are 12.8^2 km^2 and 1593.75 m, respectively. The isotropic diffusion approach refers to the application of Eq. (10), whereas the anisotropic diffusion approach allows for different values in the vertical and horizontal directions according to Eqs. (11) and (12), respectively.

3.1 Initial and boundary conditions

The CBL is forced by constant homogeneous surface fluxes $\overline{w'\theta'}_{\mathrm{sfc}} = 0.1\mathrm{mKs}^{-1}$ and $\overline{w'q'_{\mathrm{v}}}_{\mathrm{sfc}} = 2{\times}10^{-5}(\mathrm{kg\,kg}^{-1})\mathrm{ms}^{-1}$. The initial potential temperature and water vapor specific humidity are constant with values of 293 K and $8\,\mathrm{g\,kg}^{-1}$, respectively, up to the top of the boundary layer that is located at a height of 493.75 m. The inversion layer with initial thickness of 12.5 m has initial jump values $\Delta\theta = 5.04\,\mathrm{K}$ and $\Delta q_{\mathrm{v}} = -4\mathrm{g\,kg}^{-1}$. The free tropospheric humidity is set to a constant value of $4\ \mathrm{g\,kg}^{-1}$, whereas the vertical gradient of θ is set to $6\ \mathrm{K\,km}^{-1}$ above the inversion layer. The geostrophic wind is constant with height $(U_{\mathrm{g}}, V_{\mathrm{g}}) = (1, 0)\,\mathrm{ms}^{-1}$, and the initial horizontal wind is set equal to the geostrophic wind. To spin up turbulence random perturbations with maximum values of 0.1 K and $10^{-3}\,\mathrm{g\,kg}^{-1}$ were added to the initial fields of θ and q_{v}, respectively. A constant value of $1\ \mathrm{m}^2\mathrm{s}^{-2}$ for the initial subgrid TKE in the boundary layer is prescribed.

3.2 Grid configurations

A reference simulation was performed with $\Delta x_{\mathrm{hor}} = \Delta z = 12.5\,\mathrm{m}$. Table 3.1 gives a summary of the sensitivity experiments. The grid anisotropy factor r was gradually increased by systematically doubling the horizontal grid spacings from 25 up to 800 m while maintaining the same domain size (12.8 km in both horizontal directions) and vertical grid spacing ($\Delta z = 12.5$ m). We note that the extremely large grid anisotropy values were merely applied to explore different behaviours in the isotropic and anisotropic diffusivities. Because of the fixed horizontal domain size the simulations with a stretched horizontal grid were performed with a reduced number of grid points in the horizontal directions, down to only 16^2 for the coarsest cases. As a check to verify whether this choice did not impact the results, the simulations were also repeated with a minimum number of 128 grid points in both horizontal directions. We found that the latter results were qualitatively similar in terms of the mean state, turbulent flux profiles and visualizations of instantaneous fields. All simulations were performed with a variance-preserving second-order advection scheme.

4 Results

Here we will compare the results of the runs in terms of the representation of the mean state, the vertical profiles of the turbulent fluxes of heat and moisture, and tur-

bulence. We will discuss how the entrainment rate at the top of the boundary layer is affected by the particular choice of the eddy diffusion approach. The second part of the analysis will focus on the organization of turbulent structures by a visual inspection of some fields in the middle of the boundary layer in addition to a quantification of the spectral energy densities.

4.1 Mean state and turbulence structure

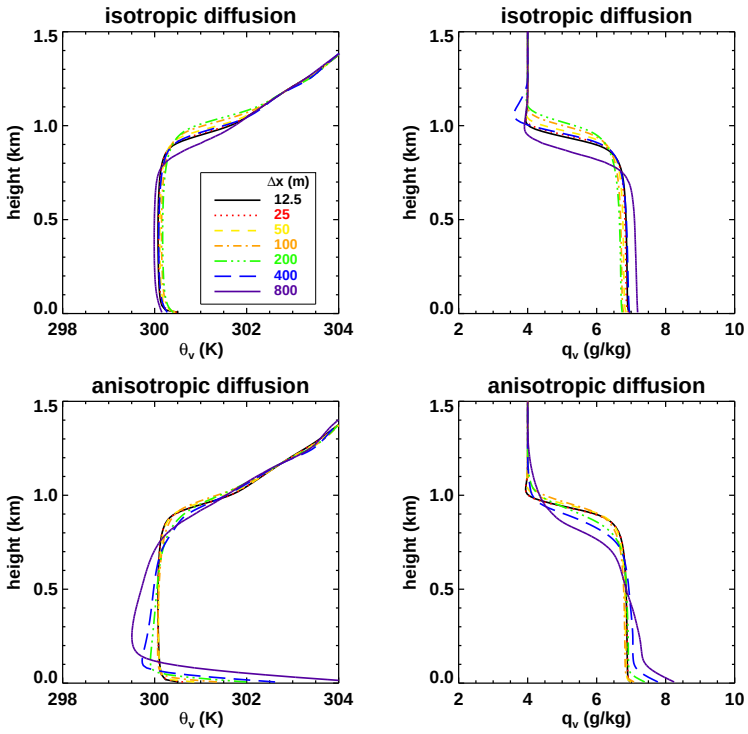

Figure 1. Vertical profiles of the horizontal slab mean values of the virtual potential temperature θ_v and water vapor specific humidity q_v during the 8th hour of the simulation. The two upper plots show simulation results for isotropic diffusion with l_Δ as a length scale, and the lower two plots were obtained for anisotropic diffusion. The horizontal grid spacings are according to the legend.

Figure 1 compares the mean state results of the virtual potential temperature θ_v and the water vapor specific humidity q_v as obtained with different horizontal grid spacings. For $\Delta x_{hor} \leq 100$ m the mean vertical profiles for θ_v and q_v in the boundary layer remain very close to the Reference run results.

The isotropic diffusion approach tends to produce slightly deeper, drier and warmer boundary layers for anisotropic grid spacings up to $\Delta x_{hor} \leq 200$ m. These deviations from the Reference case results can be explained from the relation between the growth rate of boundary layer depth (h) and the entrainment velocity (w_e),

$$\frac{dh}{dt} = w_e. \tag{23}$$

Entrainment is a process in which turbulent eddies penetrate into the inversion layer, and subsequently engulf and mix some of the relatively warm and dry inversion air downwards into the boundary layer (Sullivan et al., 1998). Larger entrainment rates therefore explain why deeper boundary layers tend to be relatively warmer and drier. For $r \leq$

16 enhanced entrainment rates might be explained from the fact that, according to Eq. (18), the isotropic eddy diffusivity will tend to increase for increasing grid anisotropy factor r.

The application of extreme anisotropic grids, $\Delta x_{\mathrm{hor}} \geq 400$ m, causes a slower growth of the boundary layer depth both for the isotropic and anisotropic diffusion approach. Because entrainment is driven by strong updrafts that penetrate the inversion layer, the slower growth rate of the boundary layer depth could possibly be explained by the resolved vertical velocity variances, which become notably smaller for coarsening horizontal grid spacings (see Figs. 2 and 3).

Last we note that the choice of the diffusion approach appears to affect the vertical stability of the boundary layer. Convective boundary layers are characterized by vertically well mixed states for quantities like θ_{v} and q_{v}, and such properties are well captured in the simulations with the smallest horizontal grid spacings. However, it can be seen that the simulation with $\Delta x_{\mathrm{hor}} = 800$ m and isotropic diffusion produces a distinct negative slope for θ_{v} almost up to the top of the boundary layer. By contrast the anisotropic diffusion approach exhibits an opposite behaviour in the sense that for $\Delta x_{\mathrm{hor}} \geq 200$ m the slope of θ_{v} clearly becomes positive above a height that is rather close to the ground surface.

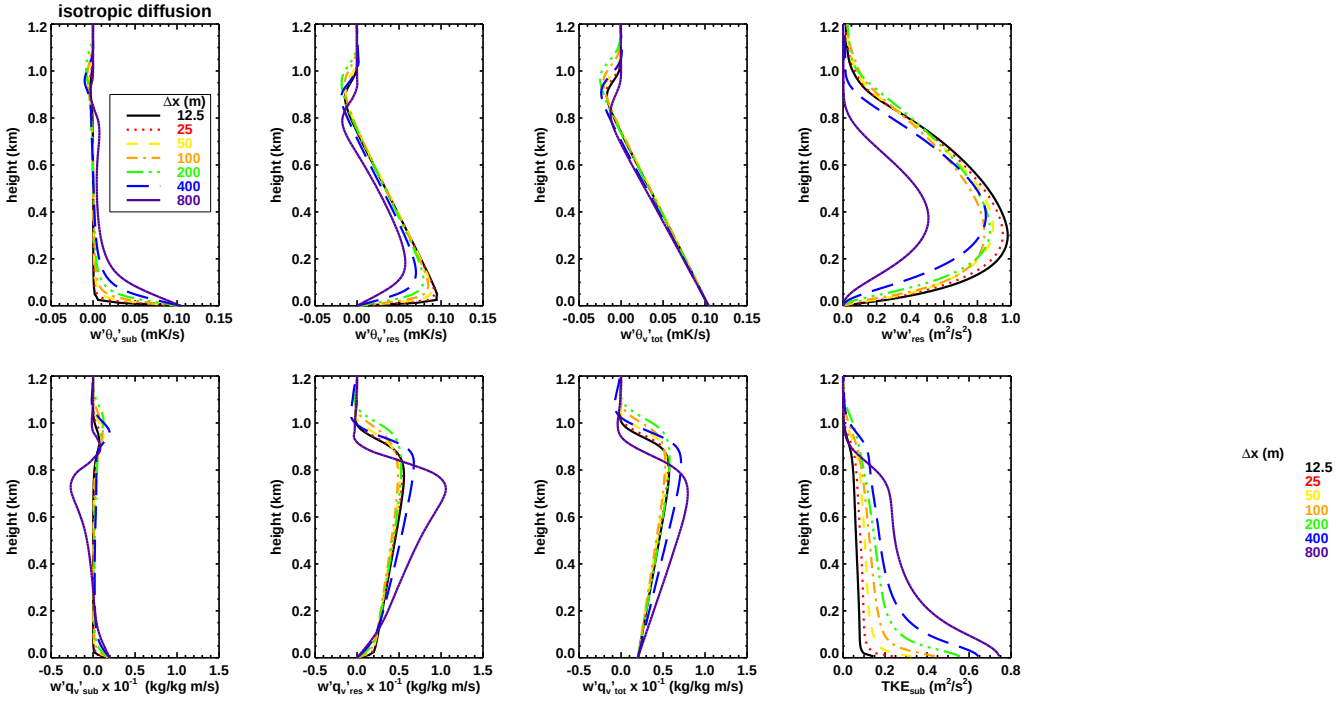

Figure 2. Vertical profiles of the vertical subgrid, resolved and total turbulent fluxes of the virtual potential temperature $\overline{w'\theta'_{\mathrm{v}}}$ and water vapor specific humidity $\overline{w'q'_{\mathrm{v}}}$, respectively, and the resolved vertical velocity variance and subgrid TKE during the 8th hour of the simulation. The results were obtained with the isotropic diffusion approach. The horizontal grid spacings are according to the legend.

Figs. 2 and 3 show vertical profiles of turbulent fluxes as obtained with the isotropic and anistropic diffusion approaches, respectively. In addition to the total ('tot') fluxes of the potential temperature and water vapor specific humidity their subgrid ('sub') and resolved ('res') contributions are also presented,

$$\overline{w'\varphi'}_{\mathrm{tot}} = \overline{w'\varphi'}_{\mathrm{sub}} + \overline{w'\varphi'}_{\mathrm{res}}. \tag{24}$$

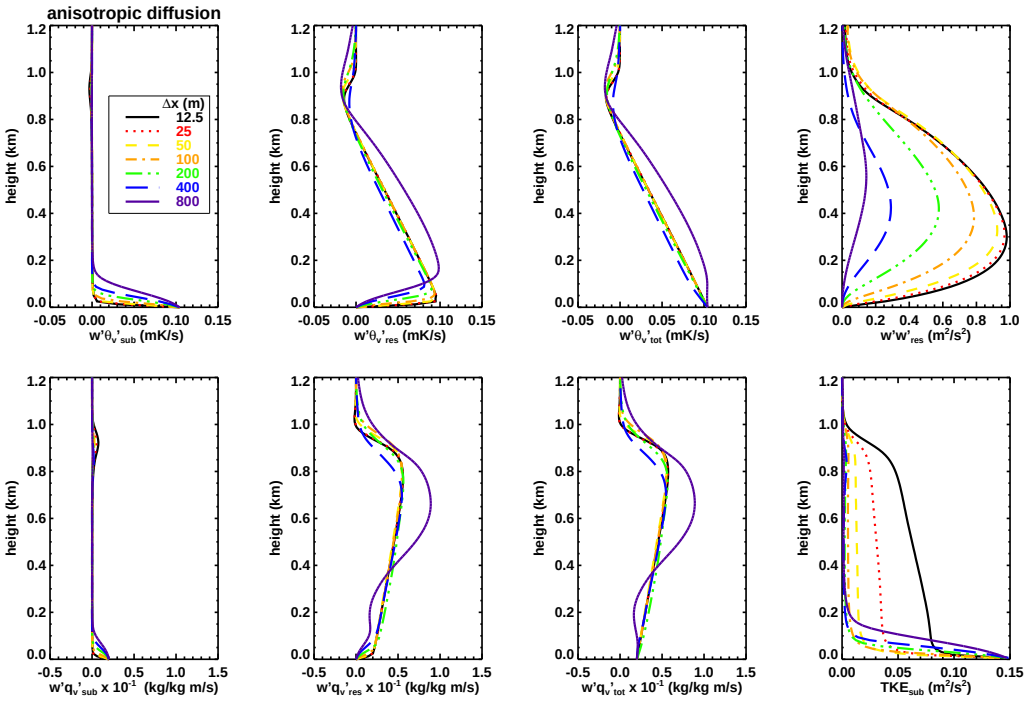

Figure 3. Similar to Fig. 2, but in the case the results were obtained with use of the anisotropic diffusion approach. Note that except for the subgrid TKE the x-axis ranges are the same as in Fig. 2.

There is a rather strong difference in the subgrid contributions to the total vertical turbulent fluxes of θ_v and q_v in the sense that for the anisotropic diffusion approach the subgrid flux contributions are mainly dominant in the lower part of the boundary layer. For the isotropic diffusion approach the subgrid fluxes become gradually more important and tend to extend towards the middle of the boundary layer for coarsening horizontal grid spacings.

Like the vertical fluxes the total turbulent kinetic energy also includes a subgrid and resolved contribution, with the latter defined as

$$\mathrm{TKE}_{\mathrm{res}} = \frac{1}{2}(\overline{u'u'}_{\mathrm{res}} + \overline{v'v'}_{\mathrm{res}} + \overline{w'w'}_{\mathrm{res}}). \tag{25}$$

With the isotropic diffusion approach the subgrid TKE tends to increase for coarsening horizontal grid spacings, and these gradual changes are accompanied by an opposing decrease of the resolved vertical velocity variance. By contrast, with the anisotropic diffusion approach both $\overline{w'w'}_{\mathrm{res}}$ and e tend to diminish simultaneously. This result is likely due to the strong stable thermal stratification that emerges if the horizontal resolution is coarsened. For example, the vertical virtual potential temperature profiles presented in Fig. 3 indicate that the boundary layer tends to become more stably stratified most notably for coarse horizontal grid spacings $\Delta x_{\mathrm{hor}} \geq 200$ m. A positive vertical gradient of θ_v acts to diminish the stability dependent subgrid factor (19). In addition, following the downgradient diffusion approach it will produce negative subgrid buoyancy fluxes. These two effects both act to diminish the subgrid TKE.

In summary, the particular kind of eddy diffusion that is applied in the simulations appears to control the subgrid TKE values. It tends to increase with coarsening hori-

zontal grid spacing for the isotropic diffusion approach, and vice versa for the anisotropic one.

The strength of the eddy diffusivity determines the dissipation of spectral energy at the smallest length scales. Because the eddy diffusivity is proportional to the square root of the subgrid TKE, and since for coarse horizontal grid spacings the latter depends strongly on the kind of diffusion approach, we will assess whether this impacts the distribution of spectral energies. Furthermore, we will analyse the organization of turbulence structures for the isotropic and anisotropic eddy diffusion approaches by a visual inspection of the instantaneous horizontal fields for some key variables.

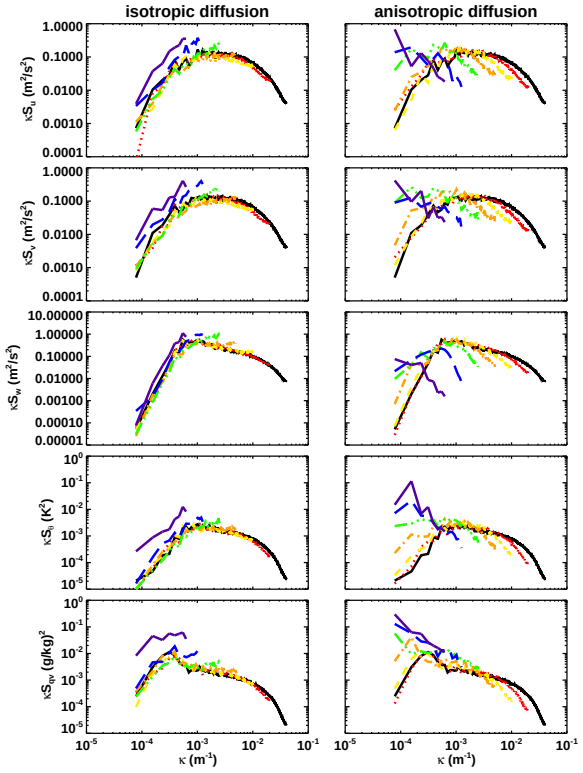

Figure 4. Spectral energy distribution for the horizontal wind components u, v, the vertical wind w, the water vapor specific humidity q_v, and the potential temperature θ, at a height of 356.25 m after 8 hours simulation time. The linestyles and colors are the same as in Fig. 3

4.2 Spatial organization

Fig. 4 presents the energy spectra of the three wind velocity components, the potential temperature and the water vapor specific humidity as a function of the wavenumber κ. The spectra were calculated from a Fourier transformation according to De Roode et al. (2004). A comparison of the results with the Reference run shows that for the anisotropic diffusivity approach a coarsening of Δx_{hor} results in a significant decrease of spectral energies at the largest wavenumbers. This suggests that the increase in the horizontal diffusivity with increasing Δx_{hor} results in a somewhat stronger dissipation at the largest wavenumbers. Interestingly, the decrease of the spectral energies at the largest wavenumbers is partially compensated by an opposite increase at the smallest wavenumbers. In other words, a coarsening of the horizontal grid spacing causes a shift of spectral energy from the largest to the smallest wavenumbers. By contrast, for coarsening horizontal grid spacings the isotropic diffusion approach tends to gives only relatively small changes in the spectral energies at the largest resolved wavenumbers. The two sets of simulations have in common that at the smallest wavenumbers the spectral energies tend to increase with respect to the Reference run, although this effect is less prominent for the isotropic diffusion approach.

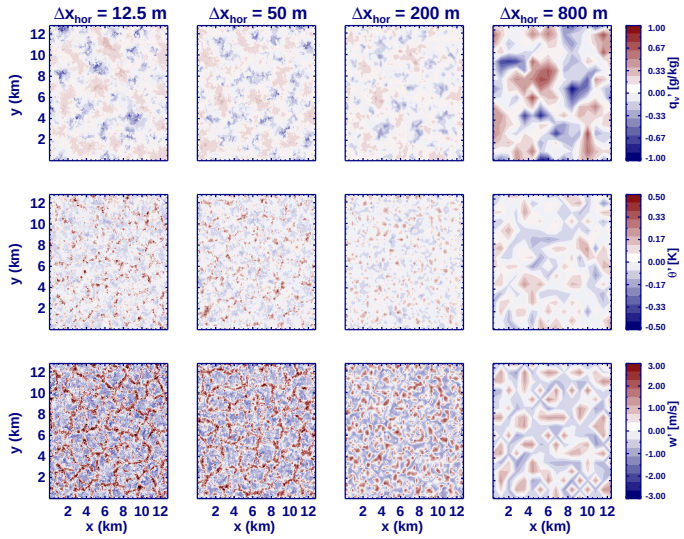

Figure 5. Contour plots of the water vapor specific humidity (upper row), the potential temperature (middle row) and the vertical velocity (lower row) at a height of 356.25 m after 8 hours simulation time as obtained from the simulations applying the isotropic diffusion approach. Each column shows the results for different horizontal grid spacings Δx_{hor}. The range of values shown in the color bars do not reflect the actual minimum and maximum values of the respective variables but are selected to provide a optimum representation of their spatial structures in addition to letting blue, white and red colors representing negative, near zero and positive values, respectively.

Fig. 5 shows snapshots of the LES fields for the isotropic diffusion approach. The turbulent structures in the simulations that applied isotropic diffusion look similar in terms of their sizes and magnitudes of the fluctuations for horizontal grid spacings Δx_{hor} up to 200 m. The fact that the dominant eddy sizes have length scales of the order of the

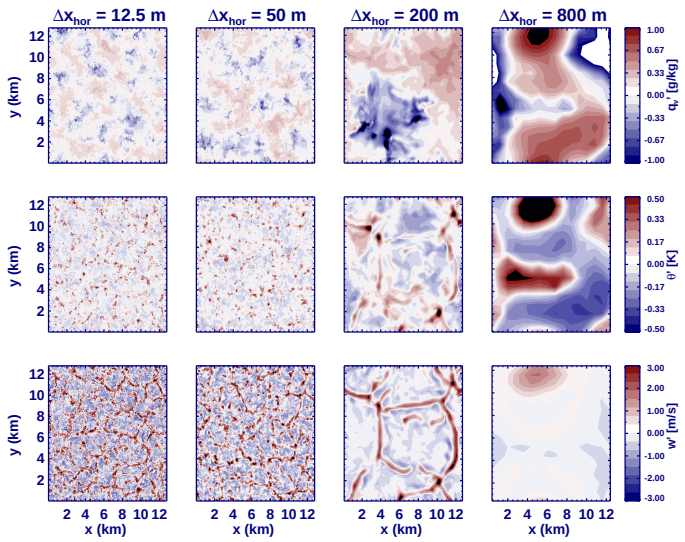

Figure 6. As in Fig. 5, but for the anisotropic diffusion approach.

boundary height, which is located near a height of about 750 m, obviously cannot be resolved with a horizontal grid spacing of 800 m, and therefore must lead to a coarsening of the spatial structures for all the three variables shown in the figure.

The loss of the spectral energy at the largest wavenumbers, and the shift of the spectral energy towards smaller wavenumbers for coarsening $\Delta x_{\rm hor}$ for the anisotropic diffusion approach as shown in Fig. 4 is clearly visible from the snapshots of the LES fields. Even for a relatively modest grid anisotropy, with $\Delta x_{\rm hor} = 200$ m, the organization of updrafts changes dramatically to a ring-like structure that is more common to cold pools that develop as a result of evaporation of rain underneath convective clouds. Also the fields of potential temperature and specific humidity become dominated by much larger structures as compared to what is found for smaller values of $\Delta x_{\rm hor}$.

We will now argue that a change in the horizontal resolution will likely have an impact on the spatial distribution of fluctuations. To this end let us consider the relation between the resolved horizontal slab mean co-variance $\overline{w'\varphi'}_{\rm res}$ of the quantities w and φ (their vertical flux), and their co-spectral energy density ($S_{w,\varphi}$) (De Roode et al., 2004),

$$\overline{w'\varphi'}_{\rm res} = \int_{\kappa_{\rm min}}^{\kappa_{\rm Ny}} S_{w,\varphi}(\kappa) d\kappa, \tag{26}$$

with the smallest wavenumber equal to the reciprocal of the horizontal domain size $\kappa_{\rm min} = 1/L_{\rm hor}$ and the Nyquist wavenumber is inversely proportional to the horizontal grid spacing $\kappa_{\rm Ny} = 1/2\Delta x$.

Let us now consider a suite of simulations in which the resolved co-variance is hardly affected by a change in the horizontal resolution. This is the case for the interior of the boundary layers in the majority of the performed runs, as is for example indicated by the vertical resolved flux profiles for, most notably, $q_{\rm v}$ in Figs. 2 and 3. If variations in the resolved flux contributions are negligibly small, or phrased differently, if $\overline{w'\varphi'}_{\rm res}$ is invariant for changes in Δx, this must consequently result in a change in the shape of the co-spectrum $S_{w,\varphi}$. The latter follows from the fact that for a coarsening horizontal grid size the integral over the co-spectrum must remain the same under the constraint

of reduced spectral wavenumber interval. Indeed, a change in Δx will result in a change of the largest wavenumber $\kappa_{\rm Ny}$ according to Eq. (26). Likewise the eddy dissipation at the largest wavenumbers can modify the co-spectra in a similar way. If a coarsening grid size is accompanied by a stronger dissipation of co-spectral energy at the largest wavenumbers, as is the case for the anisotropic diffusion approach, then conservation of co-variance requires an even stronger shift of fluctuations towards smaller wavenumbers. The vertical profiles of the total slab-mean vertical fluxes are controlled by their surface and top values. In our simulations the same surface flux values ($\overline{w'\varphi'}_{\rm sfc}$) were prescribed, but at the top of the boundary layer the fluxes ($\overline{w'\varphi'}_{\rm top}$) are controlled by the entrainment velocity ($w_{\rm e}$) according to the flux-jump relation (Lilly, 1968),

$$\overline{w'\varphi'}_{\rm top} \approx -w_{\rm e}\Delta\varphi, \tag{27}$$

with $\Delta\varphi$ the difference of the slab mean value of φ across the thermal inversion layer. In a quasi-steady state the (total) vertical flux profiles will have achieved an approximate linear profile,

$$\overline{w'\varphi'}(z) = \overline{w'\varphi'}_{\rm sfc}(1-\frac{z}{h}) + \overline{w'\varphi'}_{\rm top}\frac{z}{h}. \tag{28}$$

If the entrainment velocity is relatively insensitive to the grid configuration then this will generally result in similar vertical total flux profiles.

We recall that this insensitivity of resolved fluxes to horizontal grid size actually demonstrates an inadequacy of the subgrid TKE model for application on strongly anisotropic grids. But we believe that these results are relevant in the context of research on parameterizations for use in the Grey Zone by numerical weather prediction models. For example, a similar Smagorinsky subgrid TKE modeling approach is presently part of the hybrid turbulence closure scheme of Met Office Unified Model (Boutle et al., 2014).

5 Conclusions

We have presented LES results of a clear convective boundary for a wide range of horizontal grid spacings. Two sets of experiments with different subgrid diffusion approaches were performed. The isotropic diffusion approach applies a single local value for the eddy diffusivity in all three directions. For the Deardorff (1980a) subgrid TKE model, and with use of the mesh dependent length scale $\ell = (\Delta x\Delta y\Delta z)^{1/3}$, the isotropic eddy diffusivity can be expressed in terms of a grid anisotropy factor $r = \Delta x_{\rm hor}/\Delta z$,

$$K_{\rm m,h} \propto r^{4.3}\Delta z^2. \tag{29}$$

A similar analysis was performed for the anisotropic eddy diffusion approach, a kind of subgrid model that is, as an example, implemented in the SAM LES model. For $r > 1$ the vertical anisotropic diffusivity is smaller than the isotropic value of K_φ, but the horizontal diffusivity is larger,

$$\begin{aligned} K_{\rm m,h,vert} &\propto \Delta z^2, \\ K_{\rm m,h,hor} &\propto r^2\Delta z^2 = \Delta x^2. \end{aligned} \tag{30}$$

Note that Deardorff (1980a) suggested to use a length scale $\ell = \Delta x_{\rm hor}$ for a locally unstable atmosphere in terms of its thermal stratification, and a reduced value for stable stratifications. The use of $\Delta x_{\rm hor}$ as a length scale for the isotropic eddy diffusion approach will yield $K_\varphi \propto \Delta x^2$, similar to the value of the horizontal anisotropic diffusity.

The choice for any diffusion approach has its most notable impact on the LES results for rather coarse horizontal grid spacings. A coarsening of the horizontal grid spacing up to $r = 8$ tends to slightly enhance the entrainment velocity at the top of the boundary layer for the isotropic diffusion approach, causing slightly warmer and drier boundary layers as compared to the results as obtained with the anisotropic diffusion approach.

This finding likely is attributable to the fact that the isotropic eddy diffusivity will increase for increasing horizontal grid spacing according to Eq. (29). Because such a sensitivity is undesired, in particular as changes in temperature and humidity might affect processes like cloud formation, the use of the anisotropic diffusion approach therefore appears to be preferred for $r \leq 8$. However, for the anisotropic eddy diffusion approach it is found that an increase of the horizontal grid spacing leads to a stronger dissipation of spectral energies at the largest wavenumbers, which forces a shift in the spectral energies towards smaller wavenumbers, as evident from a stronger development of mesoscale fluctuations. As a potential remedy to this problem the formulation of the horizontal diffusivity might be modified to give somewhat reduced values with respect to the present formulation. Such a step could perhaps be taken by using inertial subrange theory as applied by Scotti et al. (1993), or, as an alternative, by the diagnosis of three-dimensional LES fields to obtain the scale-dependent horizontal and vertical eddy diffusivities like Kitamura (2015). On the other hand, the use of strong anisotropic grids for application in large-eddy simulations should better be avoided. A striking example is offered by Janssens et al. (2022). They demonstrate the impact of the representation of structures with length scales close to the mesh size on the mesoscale organization of shallow cumulus clouds.

6 Data availability statement

The code of the DALES model can be downloaded from `https://github.com/dalesteam/dales`. The data reported in this study will be made publicly available.

Acknowledgments

We would like to thank Joost Driebergen for the implementation of the first version of the anisotropic diffusion approach in DALES and Amber Nusteling for her analyses of the scale dependency of the vertical and horizontal eddy diffusivities. We thank Marat Khairoutdinov for fruitful discussions on the anisotropic diffusion approach. This work is part of the NWO-sponsored national Ruisdael program.

References

Arabas, S., Axelsen, S., Attema, J., Beets, C., Boeing, S. J., de Bruine, M., ... van Zanten, M. (2021, March). *dalesteam/dales: Dales 4.3.* Zenodo. doi: 10.5281/zenodo.4604726

Beare, R. J., Macvean, M. K., Holtslag, A. A. M., Cuxart, J., Esau, I., Golaz, J.-C., ... Sullivan, P. (2006). An intercomparison of large-eddy simulations of the stable boundary layer. *Boundary-Layer Meteorol.*, *118*, 247–272.

Boutle, I., Eyre, J., & Lock, A. (2014). Seamless stratocumulus simulation across the turbulent gray zone. *Monthly Weather Review*, *142*(4), 1655–1668.

De Roode, S. R., Duynkerke, P. G., & Jonker, H. J. J. (2004). Large eddy simulation: How large is large enough? *J. Atmos. Sci.*, *61*, 403–421.

Deardorff, J. W. (1980a). Cloud-top entrainment instability. *J. Atmos. Sci.*, *37*, 131–147.

Deardorff, J. W. (1980b). Stratocumulus-capped mixed layers derived from a three-dimensional model. *Boundary-Layer Meteorol.*, *18*, 495–527.

De Roode, S. R., Jonker, H. J., van de Wiel, B. J., Vertregt, V., & Perrin, V. (2017). A diagnosis of excessive mixing in Smagorinsky subfilter-scale turbulent kinetic energy models. *J. Atmos. Sci.*, *74*, 1495–1511. doi: 10.1175/JAS-D-16-0212.1

Doubrawa, P., & Muñoz-Esparza, D. (2020). Simulating real atmospheric boundary layers at gray-zone resolutions: How do currently available turbulence parameterizations perform? *Atmosphere*, *11*(4), 345.

Draxl, C., Allaerts, D., Quon, E., & Churchfield, M. (2021). Coupling mesoscale budget components to large-eddy simulations for wind-energy applications. *Boundary-Layer Meteorology*, *179*(1), 73–98.

Efstathiou, G., Beare, R., Osborne, S., & Lock, A. (2016). Grey zone simulations of the morning convective boundary layer development. *Journal of Geophysical Research: Atmospheres*, *121*(9), 4769–4782.

Grylls, T., Suter, I., & van Reeuwijk, M. (2020). Steady-state large-eddy simulations of convective and stable urban boundary layers. *Boundary-Layer Meteorology*, *175*(3), 309–341.

Heinze, R., Dipankar, A., Henken, C. C., Moseley, C., Sourdeval, O., Trömel, S., ... others (2017). Large-eddy simulations over germany using icon: A comprehensive evaluation. *Quarterly Journal of the Royal Meteorological Society*, *143*(702), 69–100.

Hellsten, A., Ketelsen, K., Sühring, M., Auvinen, M., Maronga, B., Knigge, C., ... Raasch, S. (2020). A nested multi-scale system implemented in the large-eddy simulation model PALM model system 6.0. *Geosci. Model Development Discussions*, 1–45.

Heus, T., van Heerwaarden, C. C., Jonker, H. J. J., Siebesma, A. P., Axelsen, S., van den Dries, K., ... Vilà-Guerau de Arellano, J. (2010). Formulation of the dutch atmospheric large-eddy simulation (DALES) and overview of its applications. *Geosci. Model Development*, *3*, 415–444. doi: 10.5194/gmd-3-415-2010

Honnert, R., Efstathiou, G. A., Beare, R. J., Ito, J., Lock, A., Neggers, R., ... Zhou, B. (2020). The atmospheric boundary layer and the "gray zone" of turbulence: A critical review. *Journal of Geophysical Research: Atmospheres*, *125*(13), e2019JD030317.

Janssens, M., de Arellano, J. V.-G., van Heerwaarden, C. C., van Stratum, B. J. H., de Roode, S. R., Siebesma, A. P., & Glassmeier, F. (2022). Spontaneous length scale growth in large-eddy simulations of mesoscale shallow cumulus fields: How fine is fine enough? *To be submitted to the J. Atm. Sci.*.

Khairoutdinov, M. K., & Randall, D. A. (2005). Cloud-resolving modeling of the ARM summer 1997 IOP: Model formulation, results, uncertainties and sensitivities. *J. Atmos. Sci.*, *60*, 607-625.

Kitamura, Y. (2015). Estimating dependence of the turbulent length scales on model resolution based on a priori analysis. *J. Atmos. Sci.*, *72*(2), 750–762.

Leonard, A. (1974). Energy cascade in large-eddy simulations of turbulent fluid flows. In *Advances in geophysics* (Vol. 18, pp. 237–248). Elsevier.

Lilly, D. (1968). Models of cloud-topped mixed layers under a strong inversion. *Quart. J. Roy. Meteorol. Soc.*, *94*, 292-309.

Mason, P. J. (1989). Large-eddy simulation of the convective atmospheric boundary layer. *J. Atmos. Sci.*, *46*, 1492–1516.

Nieuwstadt, F. T., Mason, P. J., Moeng, C.-H., & Schumann, U. (1993). Large-eddy simulation of the convective boundary layer: A comparison of four computer codes. In *Turbulent shear flows 8* (pp. 343–367). Springer.

Schalkwijk, J., Jonker, H. J., Siebesma, A. P., & Bosveld, F. C. (2015). A year-long large-eddy simulation of the weather over cabauw: An overview. *Monthly Weather Review*, *143*(3), 828–844.

Scotti, A., Meneveau, C., & Lilly, D. K. (1993). Generalized Smagorinsky model for anisotropic grids. *Physics of Fluids A: Fluid Dynamics*, *5*(9), 2306–2308.

Stevens, B., Moeng, C., Ackerman, A. S., Bretherton, C. S., Chlond, A., de Roode, S. R., ... Zhu., P. (2005). Evaluation of large-eddy simulations via observations of nocturnal marine stratocumulus. *Mon. Weather Rev.*, *133*, 1443–1462.

Sullivan, P. P., Moeng, C.-H., Stevens, B., Lenschow, D. H., & Mayor, S. D. (1998). Structure of the entrainment zone capping the convective atmospheric boundary layer. *J. Atmos. Sci.*, *55*, 3042–3064.

Van der Dussen, J. J., de Roode, S. R., Ackerman, A. S., Blossey, P. N., Bretherton, C. S., Kurowski, M. J., ... Siebesma, A. P. (2013). The GASS/EUCLIPSE model intercomparison of the stratocumulus transition as observed during ASTEX: LES results. *J. Adv. Model. Earth Syst.*, *5*, 483–499. doi: 10.1002/jame.20033

van Hooft, J. A., Baas, P., van Tiggelen, M., Ansorge, C., & van de Wiel, B. J. (2019). An idealized description for the diurnal cycle of the dry atmospheric boundary layer. *J. Atmos. Sci.*, *76*(12), 3717–3736.

VanZanten, M. C., Stevens, B., Nuijens, L., Siebesma, A. P., Ackerman, A., Burnet, F., ... Wyszogrodzki, A. (2011). Controls on precipitation and cloudiness in simulations of trade-wind cumulus as observed during RICO. *J. Adv. Model. Earth Syst.*, *3*. doi: doi:10.3894/JAMES.2011.3.5

Wing, A. A., Stauffer, C. L., Becker, T., Reed, K. A., Ahn, M.-S., Arnold, N. P., ... others (2020). Clouds and convective self-aggregation in a multimodel ensemble of radiative-convective equilibrium simulations. *J. Adv. Model. Earth Syst.*, *12*(9), e2020MS002138.

Figure 1.

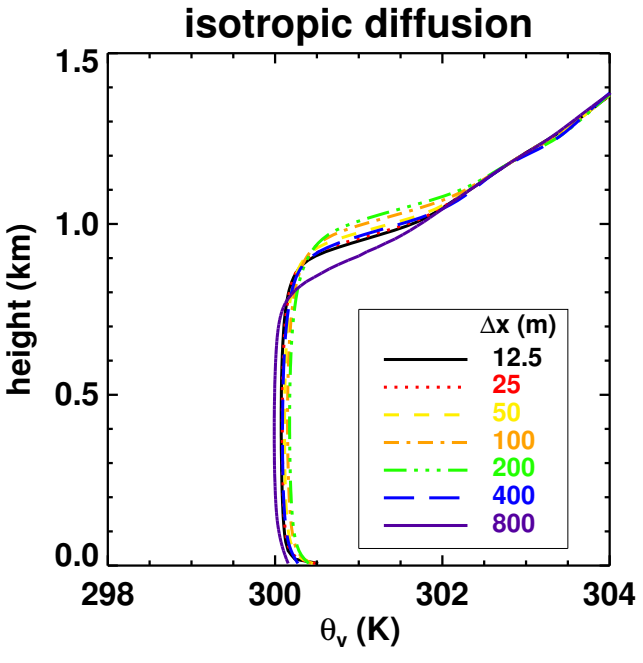
isotropic diffusion
height (km)
1.5
1.0
0.5
0.0
298
300
302
304
θv (K)
Δx (m)
12.5
25
50
100
200
400
800

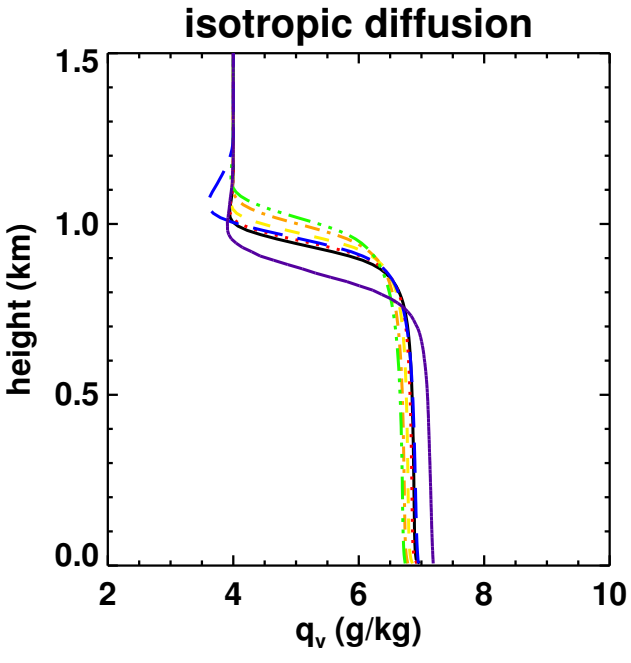
isotropic diffusion
height (km)
1.5
1.0
0.5
0.0
2
4
6
8
10
qv (g/kg)

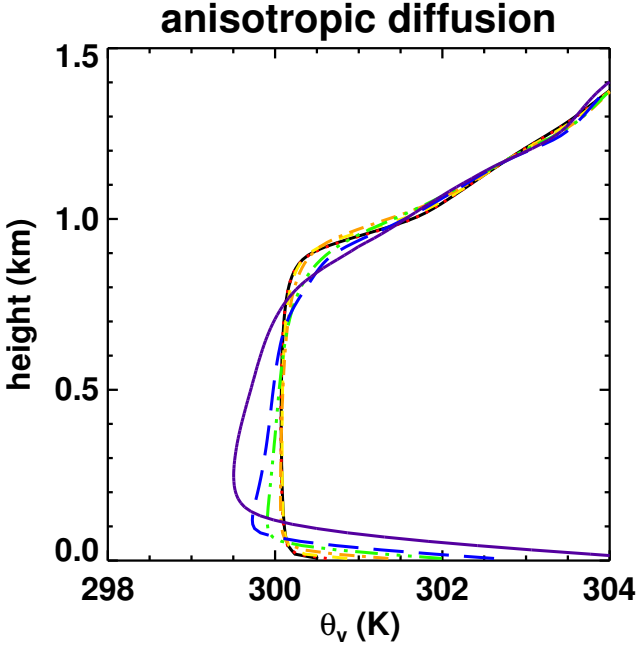
anisotropic diffusion
height (km)
1.5
1.0
0.5
0.0
298
300
302
304
θv (K)

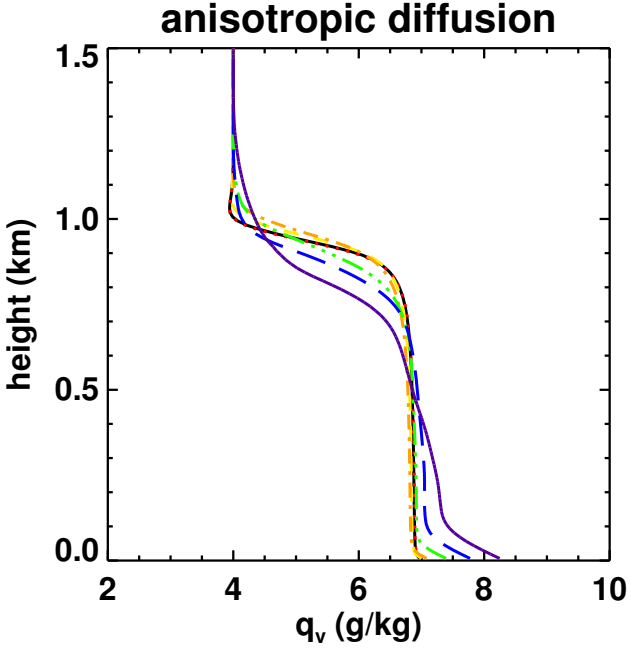
anisotropic diffusion
height (km)
1.5
1.0
0.5
0.0
2
4
6
8
10
qv (g/kg)

Figure 2.

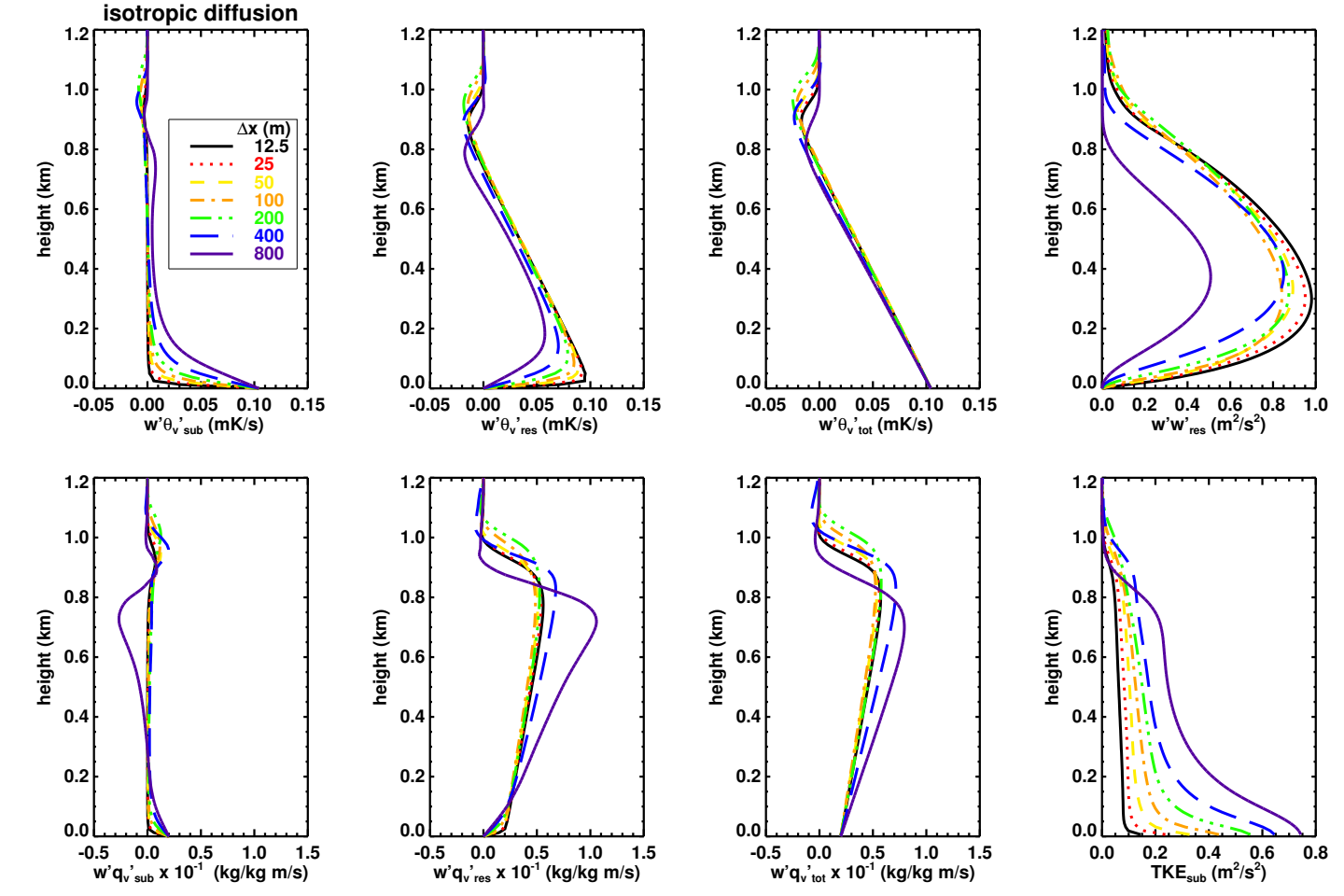
isotropic diffusion
Δx (m)
12.5
25
50
100
200
400
800
height (km)
w'θv'sub (mK/s)
w'θv'res (mK/s)
w'θv'tot (mK/s)
w'w'res (m2/s2)
w'qv'sub x 10-1 (kg/kg m/s)
w'qv'res x 10-1 (kg/kg m/s)
w'qv'tot x 10-1 (kg/kg m/s)
TKEsub (m2/s2)

Figure 3.

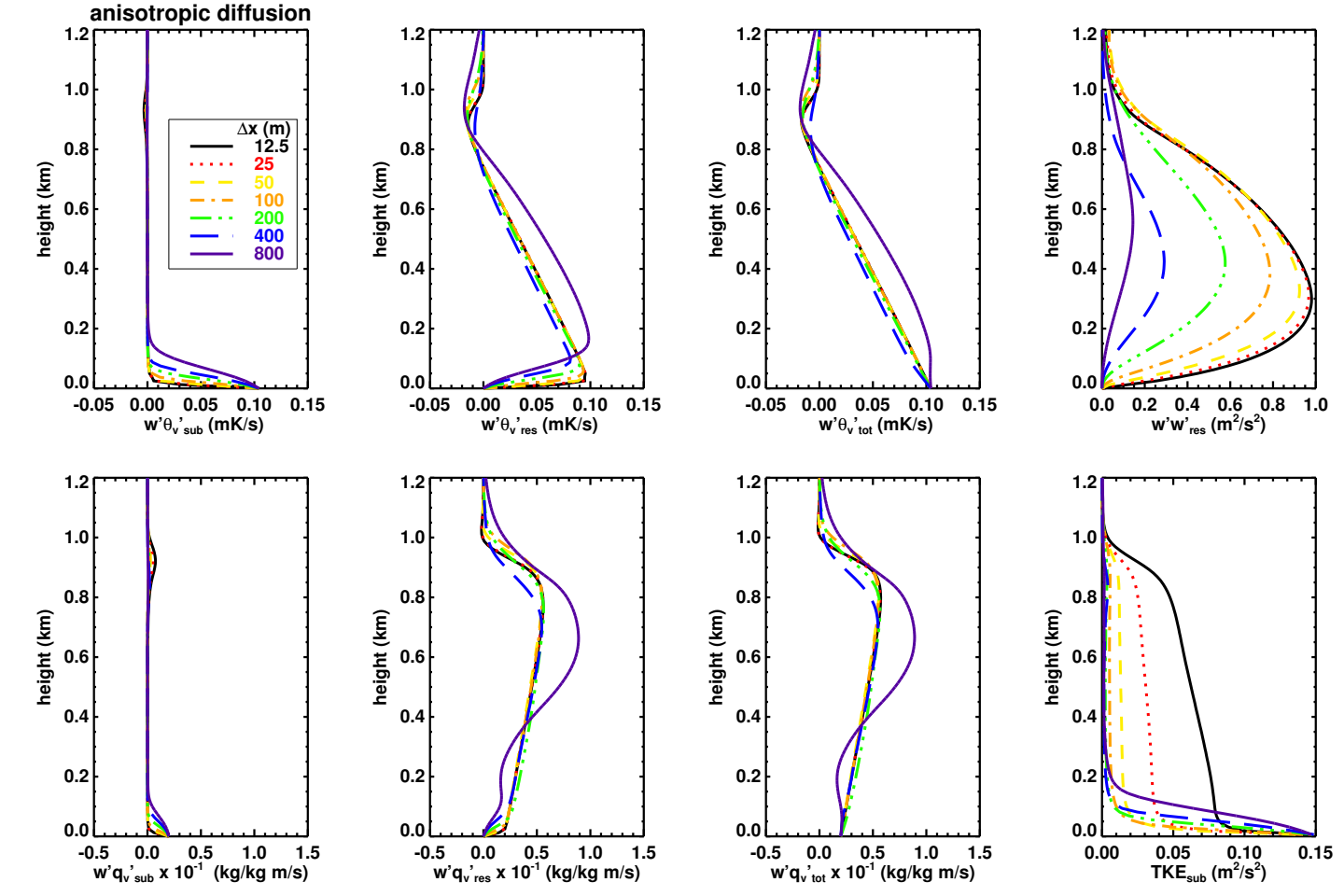
anisotropic diffusion
Δx (m)
12.5
25
50
100
200
400
800
height (km)
w'θv'sub (mK/s)
w'θv'res (mK/s)
w'θv'tot (mK/s)
w'w'res (m2/s2)
w'qv'sub x 10-1 (kg/kg m/s)
w'qv'res x 10-1 (kg/kg m/s)
w'qv'tot x 10-1 (kg/kg m/s)
TKEsub (m2/s2)

Figure 4.

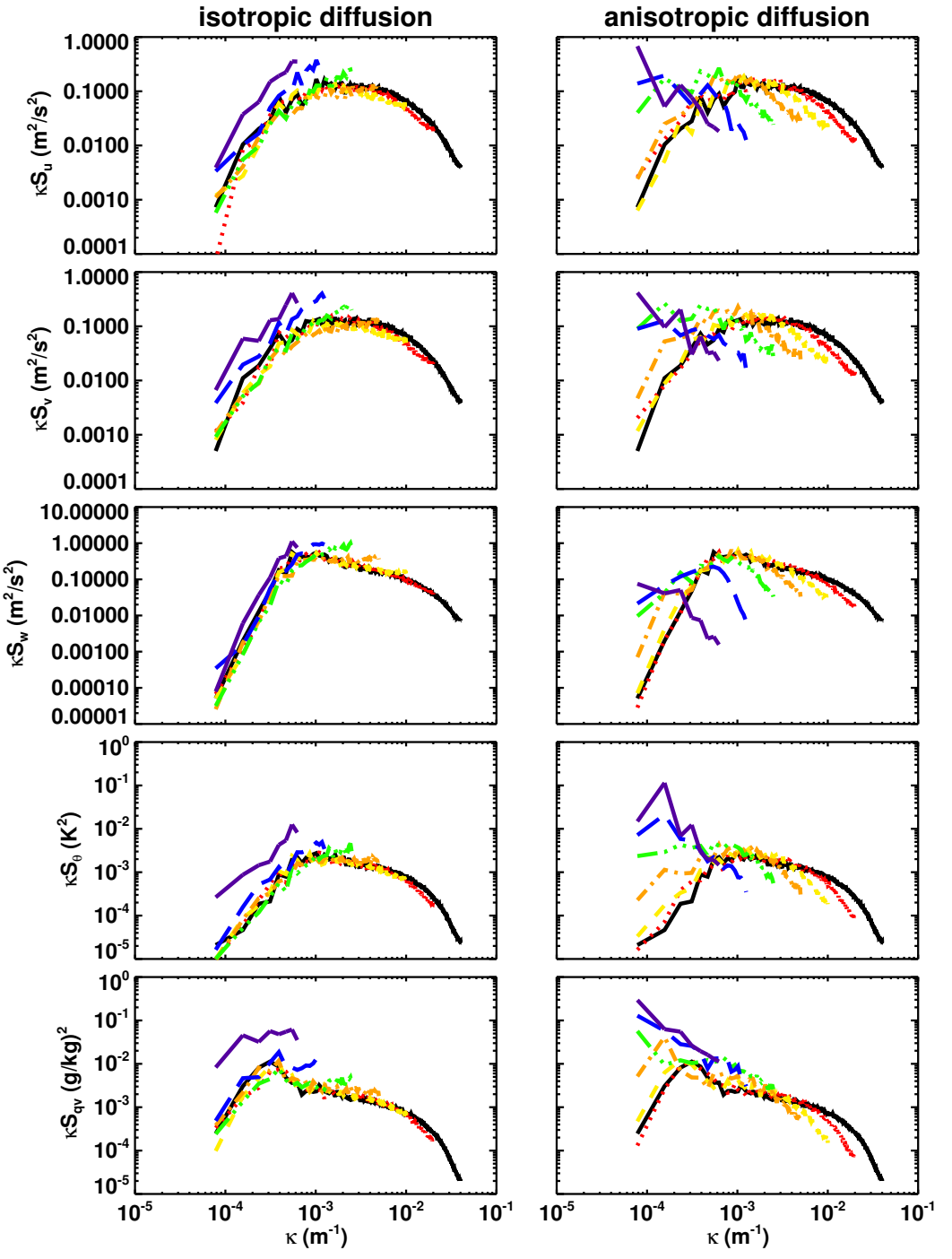
isotropic diffusion
anisotropic diffusion
κS_u (m^2/s^2)
κS_v (m^2/s^2)
κS_w (m^2/s^2)
κS_θ (K^2)
κS_qv (g/kg)^2
κ (m^-1)
κ (m^-1)

Figure 5.

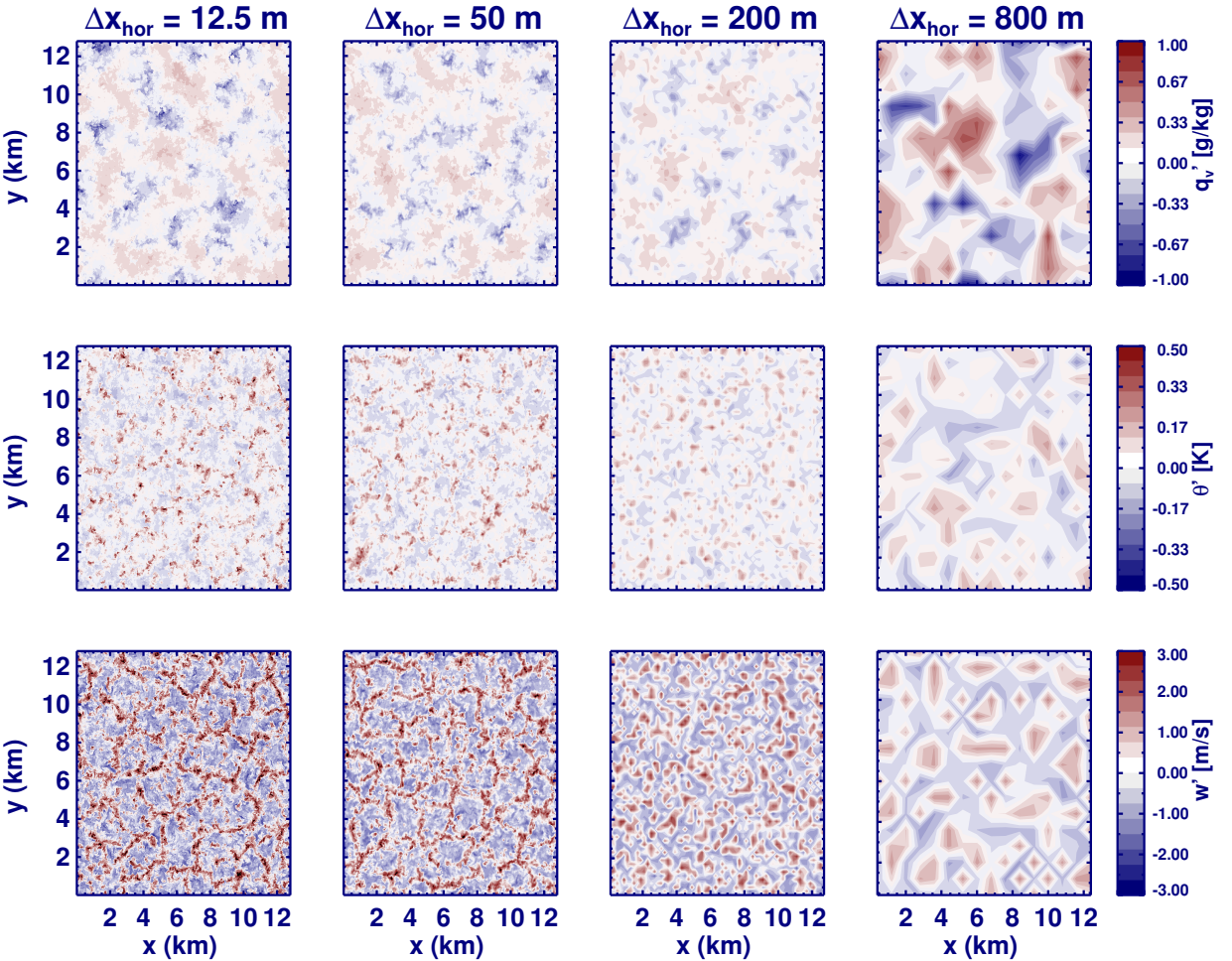
Δx_hor = 12.5 m
Δx_hor = 50 m
Δx_hor = 200 m
Δx_hor = 800 m
y (km)
x (km)
2 4 6 8 10 12
q_v' [g/kg]
1.00
0.67
0.33
0.00
-0.33
-0.67
-1.00
θ' [K]
0.50
0.33
0.17
0.00
-0.17
-0.33
-0.50
w' [m/s]
3.00
2.00
1.00
0.00
-1.00
-2.00
-3.00

Figure 6.

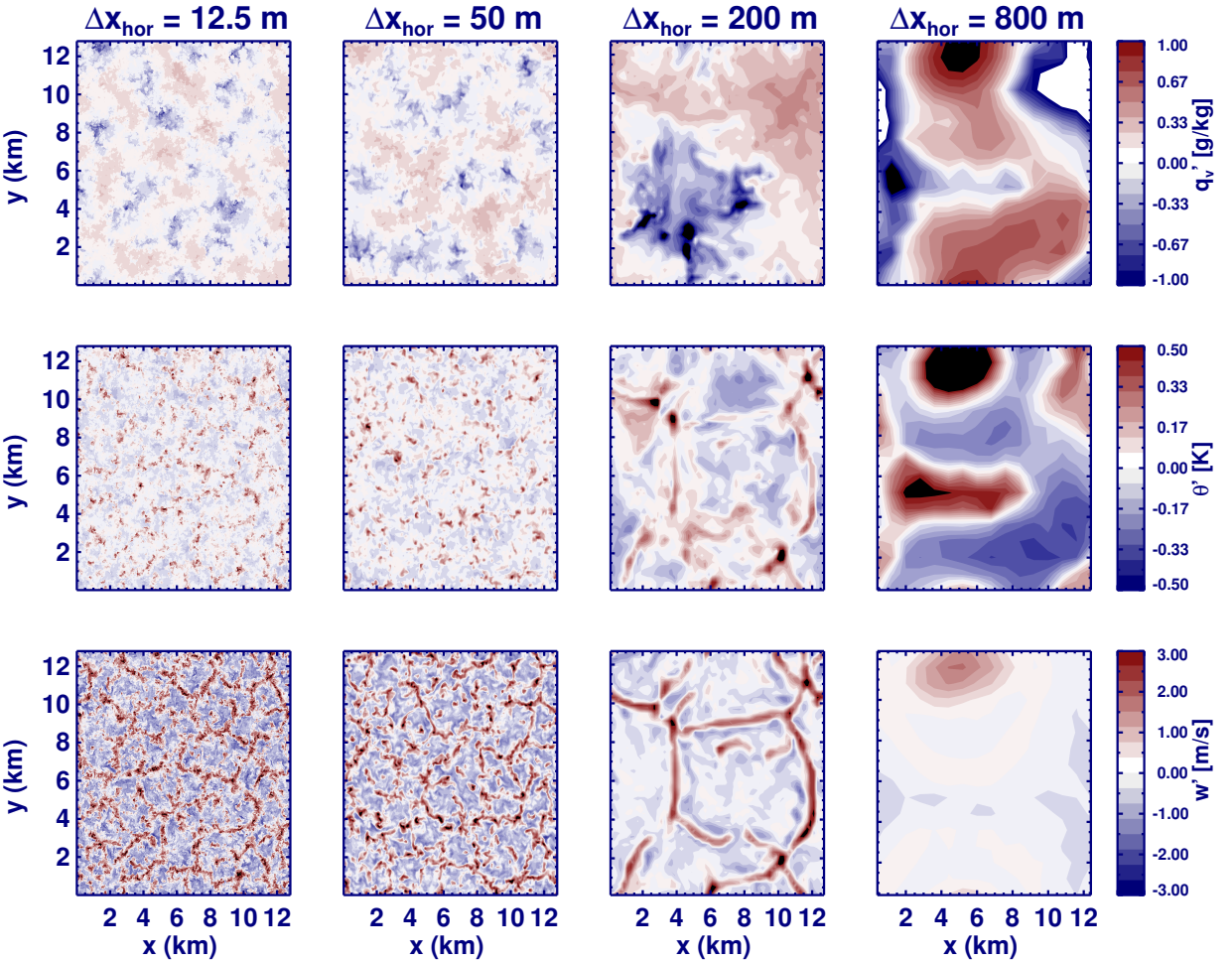
Δx_hor = 12.5 m
Δx_hor = 50 m
Δx_hor = 200 m
Δx_hor = 800 m
y (km)
x (km)
2 4 6 8 10 12
q_v' [g/kg]
1.00
0.67
0.33
0.00
-0.33
-0.67
-1.00
θ' [K]
0.50
0.33
0.17
0.00
-0.17
-0.33
-0.50
w' [m/s]
3.00
2.00
1.00
0.00
-1.00
-2.00
-3.00